Combustion and Flame 168 (2016) 127–137

Contents lists available at ScienceDirect

Combustion and Flame

journal homepage: www.elsevier.com/locate/combustflame

Measurement of the laminar burning velocity using the confined and unconfined spherical flame methods – A comparative analysis

Ahmad Omari, Leonid Tartakovsky*

Technion – Israel Institute of Technology, Technion City, Haifa 3200003, Israel

ARTICLE INFO

Article history:
Received 21 December 2015
Revised 11 March 2016
Accepted 15 March 2016

Keywords:
Laminar flame speed
Laminar burning velocity
Spherical flame
Confined flame
Flame stretch
Nonlinear stretch effects

ABSTRACT

This work investigates the consistency of experimentally determining the laminar burning velocity by using two different approaches: the unconfined flame method, based on Schlieren photography of the flame front evolution, and the confined flame method, based on pressure rise monitoring during isochoric combustion. Radiation corrected laminar burning velocity values were derived by the unconfined flame method using linear as well as non-linear stretch relations. Those values were then used as reference for evaluating the accuracy of the confined flame method. Laminar burning velocity obtained by the latter method were found to depend strongly on the modeled relation between the burned mass fraction x to the pressure P. Thus, we compare several x–P relations and show that the popular linear x–P relation overestimates the burning velocity by up to 20%. However, by "right parametrization" of a more detailed analytical x–P relation, closer results to those obtained by the unconfined flame method may be achieved. The favorable usable pressure data range for the confined flame method was also considered and found to be in the range of $(10\% < x < 55\%)$. Moreover, it was found that stretch effects are not totally negligible during the confined flame propagation, even for low Markstein length-mixtures. In summary, we suggest the analytical confined flame method as we define it in this work, to be a cost-effective and less labor-intense alternative to the unconfined flame method for applications where accuracy can be compromised.

1. Introduction

One of the probably most important parameters of a combustible mixture is its reaction rate. It dictates the heat release rate during the combustion process and is therefore of major interest in various engineering applications such as combustion engines [1], turbines, industrial burners, as well as in the fundamental studies, e.g. validation of kinetic mechanisms [2] or turbulent flame modeling [3]. Since the late 18th century, researchers have developed various experimental facilities and measuring methods to evaluate the planar laminar burning velocity (S_{u0}), being a direct representative of the reaction rate. The knowledge of the exact flame area as well as the exact mixture composition entering the flame is crucial for every burning velocity measurement method. For this reason, the spherical flame, which propagates in a homogeneous, initially quiescent air fuel mixture, has long been considered as a favorable flame structure for burning velocity determination and was considered by various researchers [4–40]. Initiated by a spark, the spherical flame propagates uniformly in all directions enabling fairly accurate determination of its area by the flame radius only. At practical laboratory conditions however, the homogeneous air–fuel mixture is usually ignited inside a closed vessel and hence the heat released during flame propagation causes a pressure raise inside the vessel accompanied also by a temperature increase of the unburned mixture. Although, it is well known that at early stages of flame propagation the pressure increase may be assumed to be negligible and hence the flame propagation is often assumed to be unconfined [13–40]. Due to this fact, two methods for measuring S_{u0} from spherical flame propagation have evolved in literature, namely the confined flame (CF) and the unconfined flame (UCF) methods. The fundamental difference between those methods is that in the former, S_{u0} is extracted from the monitored pressure rise – $P(t)$ – inside the vessel, while in the latter method S_{u0} is extracted from the flame front radius trajectory – $R_f(t)$ – usually obtained by high-speed Schlieren photography. For both methods, several modeling approaches have showed-up in literature suggesting a relation between the monitored parameters – $R_f(t)$ or $P(t)$ – to S_{u0}. In contrast to the CF method, the UCF method was vastly used in the last two decades because UCF modeling approaches have accounted for stretch effects present in the spherical flame configuration. This has reduced by far the scatter in published S_{u0} values and hence the UCF method was widely accepted as an accurate one. Although, recent studies have showed that considerable

* Corresponding author.
E-mail address: tartak@technion.ac.il (L. Tartakovsky).

http://dx.doi.org/10.1016/j.combustflame.2016.03.012
0010-2180/

Nomenclature

Greek symbols

φ	equivalence ratio
ρ	density
δ_{f0}	laminar flame thickness
ψ	relative error as defined in Eq. (26)
κ	stretch rate
$\bar{\kappa}$	mean stretch rate – time averaged

Symbols

k_u	heat capacity ratio of the unburned gas
k_b	heat capacity ratio of the burned gas
k_{br}	reduced heat capacity ratio of the burned gas – see Eq. (25)
Ka	Karlovitz number as defined: $Ka_b=\delta_f\kappa/S_{b0}$, $Ka_u=\delta_f\kappa/S_{u0}$
L_{b0}	burned gas Markstein length
L_{u0}	unburned gas Markstein length
m	mass
Ma	Markstein number as defined: $Ma_b=L_b/\delta_f$, $Ma_u=L_u/\delta_f$
P_i	initial pressure
P	pressure inside the vessel during flame propagation
P_e	adiabatic isochoric equilibrium combustion pressure
P_r	fractional pressure rise $P_r=(P-P_i)/(P_e-P_i)$
R_f	flame front radius
R_{vessel}	vessel's radius
S_{u0}	laminar burning velocity at initial conditions (plane flame)
S_{b0}	laminar burned gas velocity at initial conditions (plane flame)
$S_{u0\text{-}streched}$	stretched laminar burning velocity at initial conditions
$S_{b0\text{-}streched}$	stretched laminar burned gas velocity at initial conditions
S_u	Lam. Bur. velocity at elevated temperature and pressure
S_f	flame front velocity (displacement velocity of the flame)
S_g	burned gas expansion velocity
T_u	unburned gas temperature
T_i	initial temperature
T_b	average burned gas temperature during combustion
T_e	average burned gas temperature after adiabatic Isochoric equilibrium combustion
x	burned mass fraction

Subscripts

cf-i	confined method – "*i*" indicates number
ucf-i	unconfined method – "*i*" indicates number
u	unburned gas at any temperature and pressure
b	burned gas at any temperature and pressure
u0	unburned gas at initial conditions
b0	burned gas property at isobaric combustion
i	initial
e	burned gas property at end of isochoric combustion

uncertainties are still present due to radiation [4–9], confinement [9–18], and preferential mass diffusion effects [5], which are not accounted for in analytical UCF modeling approaches used to extract S_{u0} values from the measured data. The slight pressure rise due to confinement and in particular heat loss by radiation from the burned gas zone contribute both to an continuous increase of the burned gas density and thus to an inward flow of the expanded burned gas [4,5,8]. Thereby, the stationary burned gas assumption made in the Schlieren-based UCF models is violated. To avoid this shortcoming, high-speed particle image velocimetry (PIV) may be used to directly capture the burning velocity relative to the unburned gas [10,11], thus eliminating any assumptions regarding the burned gas. Such complication of the experimental setup are unavoidable when highly accurate S_{u0} values are desired, especially for kinetic models validation [8].

Considering the above, it is clear that increasing the accuracy in measured S_{u0} values increases considerably the experimental facility's cost as well as data processing complexity. For many engineering applications e.g. conceptual thermodynamic analysis of combustion devices, the high accuracy in S_{u0} is not critical. Instead, a labor- and cost-effective burning velocity measuring method could be of favor. This in turn could allow conducting larger numbers of experiments enabling to investigate diverse fuel mixtures and combinations, which are getting more and more important in the race for alternative fuels. In contrast to the UCF method, the CF method does not require high-speed imaging facility nor image processing techniques and is therefore considered by some authors as a cost -effective alternative to the UCF method. However, the CF modeling approaches are less investigated in literature and make by far more assumptions than the UCF models do. In this context, the main goal of this work is to assess the accuracy of burning velocity values obtained by the CF method, compared to those of the UCF method. Such a validation of the CF method has not been sufficiently carried out yet and may be of interest for users seeking to measure a laminar burning velocity cost-effectively compromising a high level of accuracy. Recent work considering confined flame approaches [22–26] usually relayed on detailed numerical simulation to evaluate the burned mass fraction and hence the flame radii from the measured pressure history. However, a recent work of Luijten et al. [27] showed that by making slight modifications to a simple analytical relation between the burned mass fraction and the pressure rise, similar results can be obtained compared to those of numerical modeling. This provoked the question: whether modifying the analytical x–P relation presented in [27] may improve accuracy of S_{u0} values derived by the CF method while still taking advantage of a simple analytical approach?

This work is organized as follows: The methodology section describes the method and the underlying assumptions made in the UCF vs. CF comparison process. Then, for completeness and readers convenience, the UCF (briefly) and in particular the CF modeling approaches used in this work are discussed in the respective subsections of the Methodology. Following, the experimental facility and the data analysis approach are described. Finally, resulting S_{u0} values determined by applying UCF and CF methods and their different modeling approaches are compared, and possible reasons for deviations are discussed.

2. Methodology

The used combustion vessel (Section 2.3) was designed to fulfill both the CF and UCF model assumptions, and hence allowed applying both methods on the same experiment. In this way, uncertainties caused by mixture preparation inaccuracies [7], like initial temperature and pressure, air–fuel ratio, fuel composition and O_2:N_2 ratio, were avoided in the comparison between the CF and UCF methods. The UCF method used with Schlieren imaging was assumed to reveal more accurate results and hence S_{u0} values derived by using it were considered as reference in evaluating the CF method's accuracy. To minimize the unavoidable uncertainties in the Schlieren-based UCF method caused by

radiation and confinement, several measures were undertaken. First, near-flammability-limit mixtures with low burning velocity were avoided [9]. Second, to minimize radiation uncertainty, flame radii were limited to <2 cm [4] and the radiation correction correlation suggested by Yu et al. [4] was used to obtain radiation-free S_{u0}'s. Third, confinement effects were minimized by limiting the used flame radii to 30% of the vessels radius [18,19]. Similar, ignition effects were eliminated by using flame radii starting from ~8 mm [20,21]. Methane–hydrogen mixtures were chosen for their low carbon number to mitigate uncertainties caused by preferential mass diffusion [5], as well as for their near-unity Lewis number [8] to avoid strong nonlinear response to stretch. Despite this fact, non-linear stretch relations were still used. In fact, four UCF stretch models were used to extract the burning velocity for the following reasons. First: to compare S_{u0} values extracted by different stretch relations, similar to previous works [12–17]. Second: to assess when the burned gas inward flow became significant. This was referred to the point where S_{u0} determined by the four UCF models started to deviate, indicating a nonlinear behavior of the stretched flame speed, that would have in worst case resulted from the non-linear effect of radiation and confinement [4,5,9,19,15].

As to the CF method, three different relations were used to evaluate the burned mass fraction (x) from the pressure rise (P) measurement. First we use the popular linear x–P approximation proposed by Lewis and von Elbe [49]. Second a more accurate analytical x–P relation suggested by Luijten et al. [27] was used and third, the latter x–P relation was used again, but with slight modification to account for more detailed chemistry, thermodynamics and radiation losses.

2.1. The unconfined spherical flame method

As the name unveils, the UCF method assumes a spherical flame propagating freely in a homogeneous air fuel mixture i.e. constant pressure and temperature of unburned gas. When neglecting confinement in real experiments as well as radiation heat loss, the burned gas generated behind the spherical flame is stationary and hence the flame front speed dR_f/dt is equal to the burned gas velocity exiting the flame. In contrast to the planar flame, the propagating spherical flame front is subtracted to surfaces stretch as it changes its area and curvature continuously. This stretching is long known to affect the thermo-diffusive and hydrodynamic nature within and ahead of the flame and hence, the actual burning velocity and flame thickness are affected too. The main goal of the various UCF modeling approaches that are discussed hereinafter, is to provide a relationship between the stretched laminar burning velocities ($S_{u0\text{-}stretch}$ and $S_{b0\text{-}stretched}$) measured in experiments, to the unstretched ones (S_{u0} and S_{b0}). Such relations are called hereinafter as unconfined flame modes. Among the pioneers of this topic, Markstein [28,29] proposed the following empirical relation:

$$S_{u0-stretched} = S_{u0} - L_{u0}\frac{2S_{b0}}{R_f} \tag{1}$$

where L_u is a measure to quantify the thermo-diffusive effect on burning velocity, the so called unburned Markstein length. Later, Frankel and Sivashinsky [30] have solved the governing conservation equations for a spherical propagating flame (continuity + species conservation + enthalpy) up to first order, i.e. neglecting terms of $O(1/R_f^2)$ – and obtained Eq.(1) analytically. They also obtained a similar relation in terms of the burned gas velocity [30] denoted hereinafter as unconfined flame model 2 "ucf-2":

$$S_{b0-stretched} = S_{b0} - L_{b0}\frac{2S_{b0}}{R_f} \tag{2}$$

where L_b is the burned Markstein length (mathematical expressions for Markstein lengths are given in Appendix A). Clavin [31] solved the conservation equations (also up to first order) in a more general manner, and proposed Eqs. (3) and (4) – denoted hereinafter as "ucf-1".

$$S_{u0-stretched} = S_{u0} - L_{u0}\kappa \tag{3}$$

$$S_{b0-streched} = S_{b0} - L_{b0}\kappa, \tag{4}$$

where κ is the stretch rate of a surface element as defined by Karlovitz [32]:

$$\kappa = \frac{1}{A_f}\frac{dA_f}{dt} = \frac{1}{4\pi R_f^2}\frac{d(4\pi R_f^2)}{dt} = \frac{2}{R_f}\frac{dR_f}{dt} \tag{5}$$

For unconfined spherical expanding flames, $dR_f/dt = S_{b0\text{-}stretched}$ and hence Eq. (5) can be written as: $\kappa = 2S_{b0\text{-}stretched}/R_f$. Thus, the difference between Eqs. (1) and (2) and Eqs. (3) and (4) lies in the definition of the stretch rate κ, where the former consider it as $\kappa = 2S_{b0}/R_f$, i.e. the rate of flame curvature change. Nevertheless, Eq. (4) in combination with Eq. (5) were widely accepted and used in the last decade [36–42]. One reason for that may be referred to its linear form which simplifies the data fitting procedure.

It is worth mentioning here that Eq. (3) cannot be converted into Eq. (4) simply by multiplying it by the density ratio (ρ_{u0}/ρ_{b0}) as it is frequently done [41,42]. In contrast to the relation $S_{b0} = (\rho_{u0}/\rho_{b0})S_{u0}$, $S_{b0\text{-}streched} \neq (\rho_{u0}/\rho_{b0})S_{u0\text{-}streched}$ and $L_{b0} \neq (\rho_{u0}/\rho_{b0})L_{u0}$. According to the definition of L_{b0} and L_{u0} in [30,31], the following relations can be derived – see Appendix A:

$$L_{u0} = \frac{\rho_{b0}}{\rho_{u0}}L_{b0} + \delta_{f0}\ln\left(\frac{\rho_{u0}}{\rho_{b0}}\right) \equiv \frac{\rho_{b0}}{\rho_{u0}}L_{b0} + L_{ex} \tag{6}$$

$$S_{u0-stretched} = \frac{\rho_{b0}}{\rho_{u0}}S_{b0-stretched} + \delta_{f0}\ln\left(\frac{\rho_{u0}}{\rho_{b0}}\right)\kappa \tag{7}$$

In contrast to L_{u0} and L_{b0} which reflect the thermo-diffusive nature of the mixture, $L_{ex} = \delta_{f0}\ln(\rho_{u0}/\rho_{b0})$ is a length parameter associated with the flames expansion ratio and thickness.

Nevertheless, the derivations of Eqs. (1)–(4) were done for the case: $S_{u0\text{-}streched}/S_{u0} \sim 1$. This simplifying assumption limits the equations to either weakly stretched flames ($\kappa \to 0$) or mixtures with $L_u \to 0/L_b \to 0$. To avoid these limitations, Frankel and Sivashinsky [43], as well as Chen and Ju [44], further solved the conservation equations for a spherical propagating flame beyond first order and obtained the following non-linear model ("ucf-3"):

$$\left(\frac{S_{b0-streched}}{S_{b0}}\right)^2 \ln\left(\left(\frac{S_{b0-streched}}{S_{b0}}\right)^2\right) = -\frac{2L_{b0}\kappa}{S_{b0}} \tag{8}$$

A further improvement up on Eq. (8) was proposed by Ronney and Sivashinsky [45] which withdraw the quasi-steady-state assumption ($d/dt = 0$) within the coordinate system attached to the moving flame front. They proposed the following non-linear non-steady model ("ucf-4"):

$$\left(\frac{S_{b0-streched}}{S_{b0}}\right)^2 \ln\left(\left(\frac{S_{b0-streched}}{S_{b0}}\right)^2\right) = \frac{1}{S_{b0}}\frac{dS_{b0-streched}}{dR_f} - \frac{2L_b\kappa}{S_{b0}} \tag{9}$$

Eqs. (9) and (8) were also obtained in their unburned gas forms by Kelley et al. [17]. As can be seen, the unsteady phenomena are introduced through the term $dS_{b0\text{-}stretched}/dR_f$. By neglecting it Eq. (9) reduces to Eq. (8). It also can be shown that when the right-hand side of Eq. (8) vanishes, it reduces to Eq. (4) [13,16,15]. Nevertheless, in contrast to the linear stretch relation, the nonlinear stretch relations – Eqs. (2), (8) and (9) – impose difficulties when fitting experimental data to obtain S_{b0}. Therefore, following Kelley et al. [17], we use them in their integrated forms. Those can be

obtained by expanding Eqs. (2), (8) and (9) into a series of inverse powers of R_f. The final integrated forms of Eqs. (2), (4), (8) and (9) are given respectively:

$$R_f + 2L_{b0}\ln\left(R_f\right) = t\cdot S_{b0} + \text{const.} \tag{10}$$

$$R_f + 2L_{b0}\ln\left(R_f\right) - 4\frac{L_{b0}^2}{R_f} - 4\frac{L_{b0}^3}{R_f^2} = t\cdot S_{b0} + \text{const.} \tag{11}$$

$$R_f + 2L_{b0}\ln\left(R_f\right) - 6\frac{L_{b0}^2}{R_f} - \frac{32}{3}\frac{L_{b0}^3}{R_f^2} = t\cdot S_{b0} + \text{const.} \tag{12}$$

$$R_f + 2L_{b0}\ln\left(R_f\right) - 4\frac{L_{b0}^2}{R_f} - \frac{8}{3}\frac{L_{b0}^3}{R_f^2} = t\cdot S_{b0} + \text{const.} \tag{13}$$

By fitting the measured $R_f(t)$ curve from the experiment to the above equations, S_{b0} and L_b are easily derived as the fitting constants. The unstretched laminar burning velocity is then calculated from S_{b0} according to: $S_{u0}=(\rho_{b0}/\rho_{u0})S_{b0}$, where the used density ratios (included in the supplementary material) were evaluated by CANTERA equilibrium calculator in this work. To counteract the underestimation in burning velocity caused by neglecting the radiation-induced inward flow of the burned gases, we use a correction equation recently suggested by Yu et al. [4]:

$$S_{u0\_RC} = S_{u0\_Ex} + 0.82S_{u0\_Ex}\left(\frac{S_{u0\_Ex}}{S_0}\right)^{-1.14} \tag{14}$$

Here S_{u0_Ex} is the burning velocity value as derived with aid of Eqs. (10)–(13), while S_{u0_Rc} is the radiation corrected value that will be used in this work.

2.2. The confined spherical flame method

The confined flame propagation differs from the unconfined one in several aspects. First, the confinement acts against the expanding burned gas and hence dR_f/dt is not equal to the burned gas velocity exiting the flame as it was assumed in the unconfined flame models. Second, the confinement implies a pressure rise which is accompanied by a temperature rise due to compression. Thus, the burned and unburned gas temperature, as well as its density, continuously increases during flame propagation. Third, in the analytical confined flame model, flame stretch is neglected, i.e. $S_{u\text{-}streched}=S_u$. This is justified by realizing that during the pressure rise period, R_f is large and the flame front speed dR_f/dt strongly reduces, thus contributing to a continuously decreasing stretch rate κ – see Eq. (5) [19,24]. Moreover, the increasing pressure may reduce the burned Markstein length, e.g., at near-stoichiometric CH_4–air mixtures, $L_b\to 0$ at $T_u=358$ K, $P=4$ bar [46], which further justifies stretch negligence for some air–fuel mixtures. With the above mentioned assumptions, the actual flame front velocity – S_f – may be expressed as the sum of the expansion velocity of the burned gas inside the flame – S_g – that pushes the flame front forward, in addition to the laminar burning velocity – S_u – at which the flame propagates into the unburned mixture:

$$S_f = S_g + S_u \tag{15}$$

where $S_u=S_u(P,T_u)$ corresponds to increasing temperature and pressure of the unburned mixture at every instance, and is not to be confused with S_{u0} which was defined at constant pressure and temperature of the unburned gas mixture. When using the confined flame model equations, S_u is extracted from the experimental data. To obtain from the latter the corresponding value of S_{u0}, the following relation may be used [22–25]:

$$\frac{S_u}{S_{u0}} = \left(\frac{T_u}{T_i}\right)^a\left(\frac{P}{P_i}\right)^b \tag{16}$$

For a constant-volume adiabatic combustion, the unburned gas temperature rises due to isentropic compression and hence Eq. (16) can be rewritten in the following form:

$$\frac{S_u}{S_{u0}} = \left(\frac{P}{P_i}\right)^\alpha \tag{17}$$

where, $\alpha=a((k_u-1)/k_u)+b$. Practically, by obtaining S_u from the experiment as function of pressure, S_{u0} can be obtained by fitting the $S_u(P)$ curve to Eq. (17) and extrapolating it back to initial pressure.

Nevertheless, Eq. (15) cannot be used directly to derive S_u because S_g cannot be obtained from direct measurement. Hence, it must be deduced from the measurable data by an appropriate modeling of the isochoric combustion process. Such confined flame modeling approaches have been developed and optimized by many researchers [47–50]. In general, by defining the laminar burning velocity as $S_u=-m_u/(\rho_u A_f)$ and the burned mass fraction as $x=m_b/(m_u+m_b)$, the following equations for the burning velocity and the flame radius may be obtained [48,38,50] .

$$S_u = \frac{dx}{dt}\frac{R_{vessel}^3}{3R_f^2}\left(\frac{P_i}{P}\right)^{1/k_u} \tag{18}$$

$$\frac{R_f}{R_{vessel}} = \left[\left(1-\left(\frac{P_i}{P}\right)^{1/k_u}(1-x)\right)\right]^{1/3} \tag{19}$$

Combining Eqs. (18) and (19) results in the following expression:

$$S_u = \frac{dR_f}{dt} - \frac{R_{vessel}^3 - R_f^3}{3Pk_uR_f^2}\frac{dP}{dt} \tag{20}$$

Eq. (20) is known as the Fiock and Marvin expression [47] and consists only from measurable parameters like pressure P and flame radius R_f. It can be easily shown that the form of Eq. (20) is identical to Eq. (15), where dR_f/dt is S_f and the second term on the right-hand side is S_g related to the pressure rise inside the vessel. However, Eq. (20) has two main drawbacks which make it practically unusable when accurate measuring of the laminar burning velocity is required. The first drawback is that S_u is obtained from subtracting two parameters of a similar magnitude ($S_f \approx S_g >> S_u$) [47]. Any error in either S_f or S_g assessment due to inaccuracies in pressure measuring or flame front position determination will strongly affect the resulting S_u. The second drawback is that it requires simultaneous and synchronized flame front filming and pressure monitoring. Both magnitudes (R_f & P) have to change considerably over the measurement period to enable the determination of fairly accurate derivatives (dR_f/dt and dP/dt). According to Eq. (19), this turns out to be only possible at flame radii between $50–70\%R_{vessel}$. However, conventional optical access (flat windows) of this size may disturb the spherical flame shape.

It is possible to develop more usable expressions for the laminar burning velocity that are free from the above mentioned drawbacks. However, this requires the knowledge of the burned mass fraction x at any time during flame propagation. Although the latter cannot be measured directly, it can be related to the pressure rise inside the vessel. Consequently, considering x to be obtainable from pressure monitoring only i.e. $x=x(P)$ and $dx/dt=(dx/dP)(dP/dt)$, O'Donovan and Rallis [48] derived the following equation from Eqs. (18) and (19), which requires pressure measuring only.

$$S_u = \frac{dP}{dt}\frac{dx}{dP}\frac{R_{vessel}}{3}\left[1-\left(\frac{P_i}{P}\right)^{1/k_u}(1-x(P))\right]^{-2/3}\left(\frac{P_i}{P}\right)^{1/k_u} \tag{21}$$

Moreover, using $x=x(P)$ in combination with Eq. (19), the stretch rate can be obtained from the measured pressure rise:

$$\kappa \equiv \frac{2}{R_f}\frac{dR_f}{dt} = \frac{dP}{dt}\frac{\frac{dx}{dP} + \frac{1}{P}\frac{1}{k_u}(1-x)}{\frac{3}{2}\left(\left(\frac{P}{P_i}\right)^{1/k_u} - (1-x)\right)} \tag{22}$$

Several efforts have been made to relate the burned mass fraction x to the pressure rise during the constant volume combustion. The most popular approach was suggested by Lewis and von Elbe [49]. They proposed a linear approximation relating x to P as follows:

$$x = \frac{P - P_i}{P_e - P_i} \tag{23}$$

This simple linear relationship is obtained however by applying two limiting assumptions and hence, Eq. (23) will be called hereafter as the linear x–P approximation. The first assumption is that the temperature of the burned gases is uniform within the burned gas zone and constant during the whole flame propagation - equal to that at the end of combustion ($T_b = T_e$). In reality, the average burned gas temperature T_b rises as the burned gases are continuously compressed due to the pressure rise inside the vessel. Moreover, the fact that burned gas residing in smaller radii shells undergoes a larger compression than the burned gas at outer shells contributes to a temperature gradient through the burned gas zone. At the end of combustion, the burned gases temperature at the center of the vessel exceeds the burned gas temperature close to the vessel's wall by up to 500 °C [22,27,51]. The second even more problematic assumption made to develop the linear x–P approximation is that the unburned gas remains at the initial temperature ($T_u = T_i$), whereas in reality it is also compressed by the expanding burned gases and thus its temperature continuously increases. Being aware of the above mentioned assumptions, Lewis and von Elbe limited their x–P approximation to the initial part of flame propagation, where $x < 1\%$ [50]. Unfortunately, Eq. (21) is unpractical for the initial part of flame propagation, where the pressure rise rate is hardly measurable. In fact, at low pressure rise, both dP/dt and the term in the square brackets vanish simultaneously ($S_u = \sim 0/\sim 0$). Hence, any measurement error would contribute to a strong overestimation or underestimation in the predicted S_u value. To avoid this problem, several authors [19,52,53] have used the linear x–P approximation in combination with Eq. (21) for $x > 1\%$ ignoring the validity range of Eq. (23).

A more accurate x–P relation that took into account the temperature rise in both the burned gas zone and the unburned gas zone was proposed by Luijten et al. [27]. They also have considered energy conservation in the whole combustion vessel and ended up with the following analytical x–P relation:

$$x = \frac{P - P_i \cdot f(P)}{P_e - P_i \cdot f(P)}$$
$$f(P) = \left(\frac{k_b - 1}{k_u - 1}\right) + \left(\frac{k_u - k_b}{k_u - 1}\right)\left(\frac{P}{P_i}\right)^{\frac{k_u - 1}{k_u}} \tag{24}$$

where k_u is the heat capacity ratio of the unburned gas and k_b – the heat capacity ratio of the burned gas. Eq. (24) is the most accurate x–P relation obtainable using analytical equations and hence is called hereafter as the 'analytical x–P relation'. It is valid over the entire flame propagation range $0 < x < 1$, or alternatively $P_i < P < P_e$. It is noted that by substituting $k_u = k_b = 1$ in Eq. (24), it reduces to the linear x–P approximation – Eq. (23).

Nevertheless, the above x–P relations – Eq. (23) and Eq. (24) – were derived using a two-zone model, where the reaction interface separates between a burned gas zone and an unburned gas zone, each with constant caloric properties. Further modifications can be made by using numerical multi-zone x–P relations that account for the previously mentioned temperature gradient in the burned gas zone as well as for temperature-dependent caloric properties and dissociation. Luijten et al. [22,27,54] investigated how various refinements, like those mentioned, affect the x–P relation. They also compared their analytical x–P relation – Eq. (24) – with numerical ones assumed to be more accurate as they capture more detailed chemistry and thermodynamics. Their results showed that there is a considerable difference between the linear x–P approximation – Eq. (23) – and the two-zone analytical x–P relation – Eq. (24) – especially at the mid-pressure range. Also, they showed that there is no detectable difference between an analytical two-zone and an analytical multi-zone model. This implies that the effect of temperature gradient within the burned gas zone is minor compared to the rise in the average burned gas temperature that was taken into account in the two-zone analytical x–P relation – Eq. (24). The numerical models, especially those which included dissociation, further deviated from the analytical x–P relations. While including dissociation strongly affects the x–P relation, changing caloric properties has showed a weaker effect. Their remarkable finding however was that further detailing the thermodynamics and chemistry in numerical models has an equivalent effect as reducing the burned gas specific heat ratio k_b used in the analytical x–P relation – Eq. (24). Moreover, when evaluating the flame front radius from Eqs. (19) and (24), it can be shown that by reducing the k_b value the resulting flame radius R_f is underestimated. Bearing in mind that radiation heat losses from the burned gas zone also contribute to a retarded expansion, it follows that by reducing the k_b parameter, a radiation-like effect may be produced. Considering the above findings, in this work we use the analytic x–P relation – Eq. (24) once with the k_b parameter corresponding to the actual burned gas state, and after that – with a reduced value of k_b (denoted as k_{br}) as an alternative to a more detailed-thermodynamic & chemistry x–P relation.

The magnitude of k_b reduction however remains questionable and is for sure individual for each case. Moreover, it also changes over the flame propagation period due to continuously changing equilibrium conditions in the burned gas zone as well as changing radiation heat loss intensity. Since detailed numerical flame propagation simulations capable of capturing some of the mentioned effects are out of the current work's scope, a case-dependent k_b reduction is not provided. Instead, a reasonable k_b reduction method was selected based on the work of Van den Bulck [55]. He shows, for example, that for stoichiometric Methane combustion a reduced k_b of 1.06–1.10 would be more appropriate than the actual $k_b \sim 1.22$. Considering the latter result and the fact that k_{br} is physically bounded in-between *1* and k_b, the following k_b reduction approach was used in this work.

$$k_{br} = \frac{1 + k_b}{2} \tag{25}$$

The required thermodynamic properties – P_e, k_u and k_b – were determined using the CANTERA equilibrium calculator. Unlike P_e which is a property at well-defined conditions, k_u and k_b change as the temperature increases due to the pressure rise and thus mean values are taken. k_u is evaluated at 400 K which corresponds to a pressure rise of $P \approx 2.9P_i$. k_b is evaluated as the average of k_b at the isochoric burned gas condition (k_{be}) and that at isobaric burned gas conditions (k_{b0}) . This averaged value – k_{ba} – is considered to correspond to the actual burned gas. The reduced k_b parameter (k_{br}) is then evaluated from k_{ba} according to Eq. (25). The values of the above mentioned parameters are given in the supplementary material.

2.3. Experimental facility

A 1-l (Ø 124.2 mm) spherical closed combustion vessel was designed for the purpose of this study. On both sides of the vessel 8 mm-thick windows were made for optical access. The

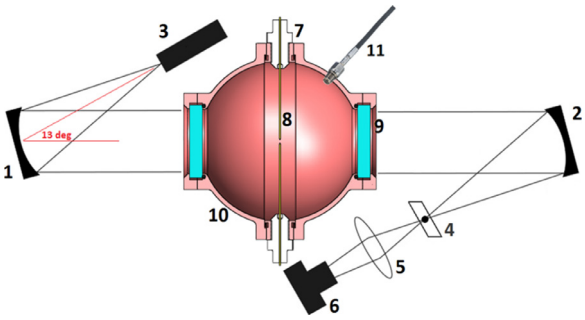

Fig. 1. Combustion vessel and Schlieren system layout. 1 – point light source, 2 and 3 – parabolic mirrors, 4 – black dot on a glass sheet, 5 – aspheric lens, 6 – camera, 7 – teflon insulation, 8 – electrodes, 9 – glass windows, 10 – combustion vessel, 11 – Pressure transducer.

windows aperture diameter is 2″ which corresponds to 40% of the vessels diameter. This was a compromise between providing windows large enough to observe the flame growth during the unconfined propagation, while keeping effect of the flat windows on the vessel's spherical shape minor enough to assume a spherical flame shape during the confined flame propagation. The vessel was made from aluminum with an anodize coating. The pressure rise was monitored using a piezoelectric pressure transducer KISTLER 7613C connected to a charge amplifier KISTLER 5010. The combustible mixtures were ignited in the center of the combustion vessel using Ø 1 mm tungsten electrodes. The spark was generated using a commercial AEM IGBT "SMART" coil. The gap between the electrodes was set to ∼1 mm. A Z-type Schlieren system was used to visualize the flame front. Two 3 in. on-axis parabolic mirrors were used. The largest possible focal length was chosen to reduce the stigmatism effect caused by using on-axis mirrors in an off-axis configuration. A 440 mW white LED light was used as a point light source. Flame propagation was filmed at 8000 fps using a PHANTOM V7 high-speed camera. A cutoff of the vessel and a scheme of the Schlieren system are shown in Fig. 1.

Instead of a knife-edge typically used to produce a Schlieren image, a Ø 3 mm black-dot was drawn on a glass sheet and located at the focal point of the second parabolic mirror. In such a way the Schlieren image was found to be sharper, brighter and with more contrast compared to the image produced using a knife edge.

All air–fuel mixtures tested in this work were prepared according to the partial-pressure technique. Fuel mixtures containing more than one component e.g., CH_4–H_2 were first premixed in a 0.8 l pre-chamber, and then mixed with air in the main combustion chamber. In contrast to pre-defining the equivalence ratio and then filling the chamber as it is commonly done in other works, the equivalence ratio of the mixture was evaluated after the filling process based on the measured partial pressures of air and fuel introduced into the combustion chamber. In this way, uncertainties from inaccurate control of the filling valves were eliminated. This filling approach did not allow reproducing identical equivalence ratios and hence repeatability test for a given equivalence ratio could not be done. Instead, repeatability was assessed by doing many experiments at different equivalence ratios (∼30 for each fuel), thereby covering the equivalence ratio range with sufficient number of measurement points. This in turn, provided a good overview of the scatter – see Figs. 6–9. Before filling the combustion vessel, it was evacuated down to 5 Torr, flushed with air to clean combustion residuals and re-evacuated. To ensure proper mixing, the vessel was first filled with the gaseous fuel followed by clean air (composed of 21% O_2 and 79% N_2). The clean air was introduced until the combustion vessel's pressure reached 0.95 bar. To reach the initial pressure requirement of approximately 1 bar, additional air was introduced from the surroundings which had a constant

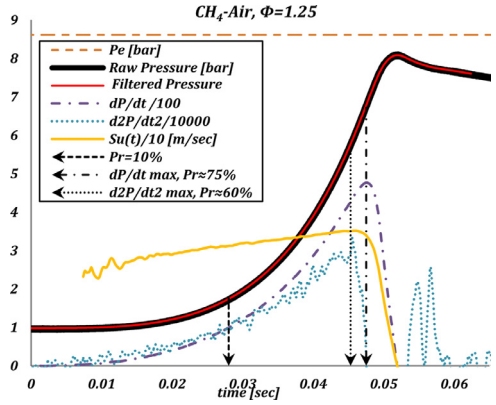

Fig. 2. Pressure history during the combustion event. The pressure curve derivatives and the Su(t) curve are also showed. (For interpretation of the references to color in this figure, the reader is referred to the web version of this article.)

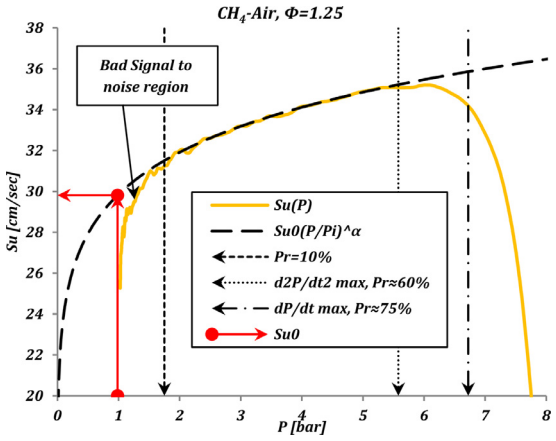

Fig. 3. Burning velocity vs. pressure inside the vessel. (For interpretation of the references to color in this figure legend, the reader is referred to the web version of this article.)

ambient pressure of 0.983 bar. Although the 1 bar target was not reached, this filling method was preferred because taking the ambient pressure as a reference allowed us to reproduce identical initial pressures, which is extremely important for the confined flame method.

2.4. Data analysis

Figure 2 shows the monitored pressure data during the whole flame propagation period. The measured raw pressure (black) was filtered with a low-pass filter and phase corrected to reduce a typical high-frequency noise caused by the data acquisition system. The pressure derivative was calculated from the filtered pressure data (red). Calculating the derivative from the raw pressure data would magnify the noise. Then, Eq. (21) along with Eq. (24) were applied on the filtered pressure data and its derivative to obtain the $S_u(P)$ curve shown in Fig. 3. The 1D laminar burning velocity at initial conditions – S_{u0} – was then obtained by fitting the $S_u(P)$ curve to Eq. (17) and extrapolating it back to the initial pressure. The pressure range used for the fitting process ($10\% < P_r < 55\%$) is indicated by the arrows in Figs. 2 and 3. The lower limit ($Pr = 10\%$) was set by two considerations. First, it has to be noted that Eq. (21) is highly sensitive to low-pressure data, because both the nominator term (dP/dt) and the denominator term (the term in the square brackets) vanish at low pressure. At the limit of $P_r \to 0$, S_u should be equal to S_{u0}. However, under practi-

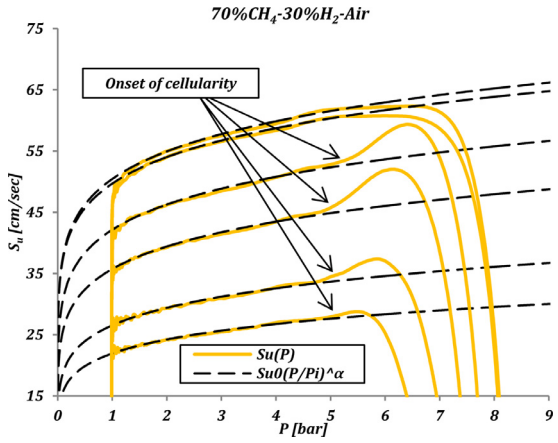

Fig. 4. Selected Su(P) curves for 70%CH_4–30%H_2–air mixtures showing rapid increase in burning velocity due to the onset of cellularity. The curves correspond to: down-up: $\Phi = 0.690$, 0.734, 0.820, 0.893, 1.046, 1.114.

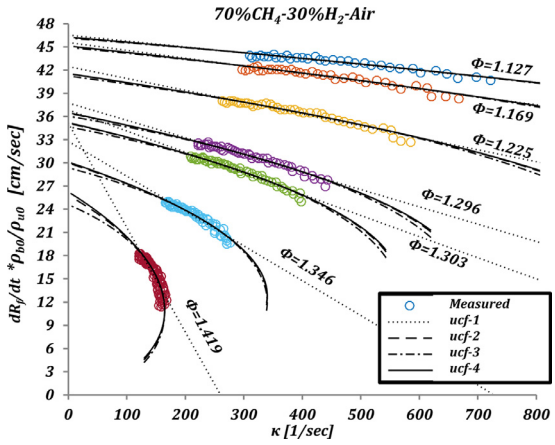

Fig. 5. Selected unconfined flame model fittings to measured data – validation of compression- and ignition – effect free data range.

cal conditions this limit cannot be reached. Any inaccuracy in dP/dt like noise or bias causes the limit to shift or even explode in some cases. Depending on the pressure-transducer's accuracy, dP/dt can be accurately determined starting from P_r>5%. The second consideration for the lower data limit is the elimination of stretch effects which are not accounted for in the confined flame method. The upper limit (P_r=55%) corresponds to the point where heat loss to the vessels wall could not be neglected anymore. In fact, the strong decrease in burning velocity observed at $P_r > 60\%$ (Figs. 2 and 3) is believed to results from to the increased heat loss to the vessel's wall caused by the closely approaching flame front ($R_f/R_{vessel} > 0.9$). The heat transfer is believed to be attributed by two main reasons. First, the large flame area at the late stages of flame propagation contributes to higher radiation heat losses, which affects the overall pressure rise in the vessel. The point where this effect becomes significant can be referred to the moment when the pressure derivative maximizes $P_r \approx 75\%$, i.e. does not continue to increase, whereas without heat loss it would – Fig. 2. The second heat transfer mechanism is a conductive heat loss from the compressed hot unburned gas residing between the flame and the vessels wall. This results in an non-isentropic compression of the unburned gas and hence the $S_u(P)$ curve does not follow the predicted path defined by Eq. (17) – (Fig. 3 – the section residing within $60\% < P_r < 75\%$). The moment where the separation of the measured $S_u(P)$ curve from eq.(17) occurred was found to correlate with the moment when the second derivative of the pressure curve maximizes - see $P_r \approx 60\%$ in Fig. 2. Consequently, $P_r \approx 55\%$ was chosen to indicate the time after which heat losses were considered not-negligible. Further reducing the upper limit may mitigate inaccuracies caused by the heat losses, but has to be compromised with the reduced usable data range available for the fitting procedure of the $S_u(P)$ curve to Eq. (17).

An additional fact worth to mention is the onset of cellularity which occurs for hydrogen-enriched mixtures. Figure 4 shows selected $S_u(P)$ curves for 70% CH_4–30% H_2–air mixtures. It can be clearly seen that for lean mixtures a rapid increase in burning velocity occurs towards the end of the combustion process. This point indicates the onset of cellularity. For rich mixtures, cellularity did not occur as anticipated. At the given experiment conditions in this work, cellularity, when it occurred, started after $P_r \approx 60\%$ and hence was out of the used data range. When cellularity is contained in the used data, it leads to overestimation of the extracted laminar burning velocity by up to 100% [56].

To obtain the laminar 1D burning velocity according to the unconfined flame method, the $R_f(t)$ curves were first obtained from the Schlieren images based on a predetermined threshold on the pixels gray-color-number. After locating the flame front, a best circle fit was made and its radius was considered as the flame radius R_f. Next, the $R_f(t)$ curve was fitted to Eqs. (10)–(13), from which S_{u0} and L_{b0} were then obtained as the fitting constants. Figure 5 shows the measured dR_f/dt in addition to extrapolated dR_f/dt curves according to Eqs. (10)–(13). It can be seen from the measured points that compression and ignition effects were not noticeable in the selected data range.

3. Results and discussion

Figures 6 and 7 show laminar burning velocity values obtained with the confined and unconfined flame methods and their different models. The $R_f(t)$ curve obtained from the Schlieren images were analyzed according to the unconfined flame models: ucf-1, ucf-2, ucf-3 and ucf-4 (Eqs. (10), (11), (12) and (13), respectively). The pressure trace $P(t)$ was analyzed according to the confined flame model – Eqs. (21) and (24) – along with three different parameterizations for the analytical x–P relation – Eq. (17): First, to reproduce the linear x–P approximation, k_u and k_b were set to zero (case cf-1). Second, the actual k_u and k_{ba} parameters of the mixture were used (case cf-2). Third, the actual k_u and the reduced k_{br} parameter were used (case cf-3).

To provide clearer insight into the differences of the burning velocity values, a parameter ψ was defined as the relative deviation from the burning velocity value derived by the non-linear

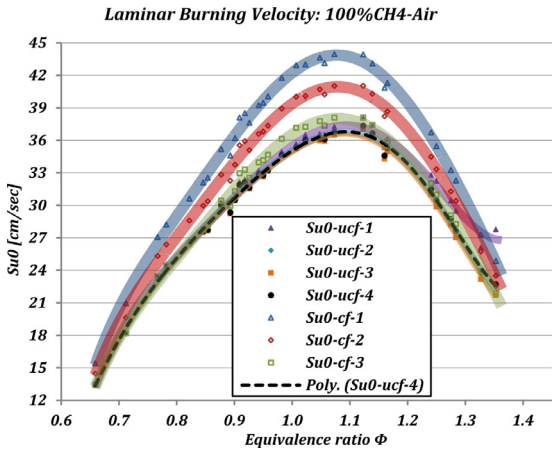

Fig. 6. Laminar burning velocities obtained by different methods for CH_4–air mixtures.

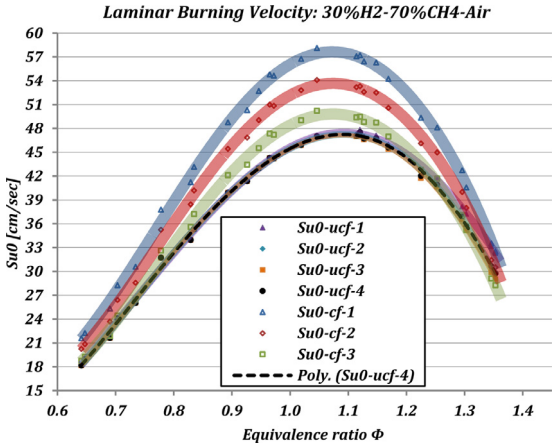

Fig. 7. Laminar burning velocities obtained by different methods for 70%CH_4–30%H_2–air mixtures.

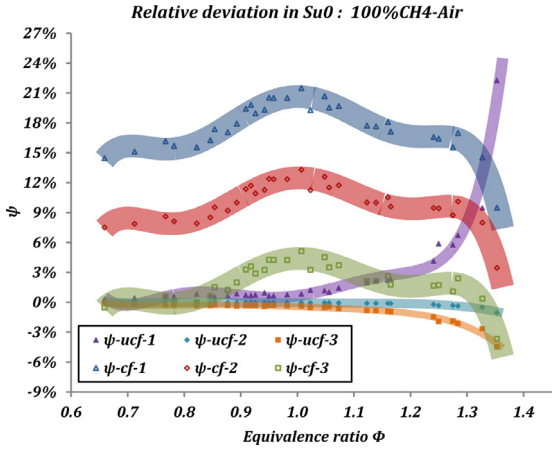

Fig. 8. Relative deviation in burning velocity obtained by different methods and models. Mixture: CH_4–air.

non-steady unconfined flame model (Eq. (13)). Bearing in mind that Eq. (13) was derived from the most detailed mathematical model, $S_{u0\text{-}ucf\text{-}4}$ is considered as the most accurate burning velocity value in this work.

$$\psi_i = \frac{S_{u0-i} - S_{u0-ucf-4}}{S_{u0-ucf-4}} \tag{26}$$

Figures 8 and 9 show the obtained ψ values for the different modeling approaches considered in this study.

The burned and unburned Markstein lengths are shown in Figs. 10 and 11. L_{b0} was directly deduced from the unconfined flame models. L_{u0} was then calculated from L_{b0} according to Eq. (6), where the necessary L_{ex} parameter was evaluated using CANTERA. As can be seen from Figs. 10 and 11, the investigated CH_4–air and CH_4–H_2–air mixtures have very low Markstein lengths ($|L_b| < 0.05$ cm) in the lean region ($\Phi < 1$). For these low burned Markstein lengths, the burning velocities obtained by all four unconfined flame model equations are almost identical, as can be seen in Figs. 8 and 9.

As the mixture gets richer and the burned Markstein length increases, it can be seen that the linear stretch relation starts to overestimate both the burning velocity and the Markstein length. In contrast, the non-linear models ucf-2, ucf-3 show closer results to ucf-4. Figure 12 shows $\psi_{\text{-}ucf\text{-}i}$ as function of $Ma_bKa_b \approx L_{b0\text{-}ucf\text{-}i} * K_{ucf\text{-}mean} / S_{b0\text{-}ucf\text{-}i} \approx L_{b0\text{-}ucf\text{-}i} / R_{f\_mean}$. As can be seen, for low values of Ma_bKa_b, the deviation resulting from different UCF models is minor. Remarkably, ucf-2, which was proposed empirically by Markstein, reveals the close results to the most detailed model – ucf-4. These results are in agreement with previous works [12,14].

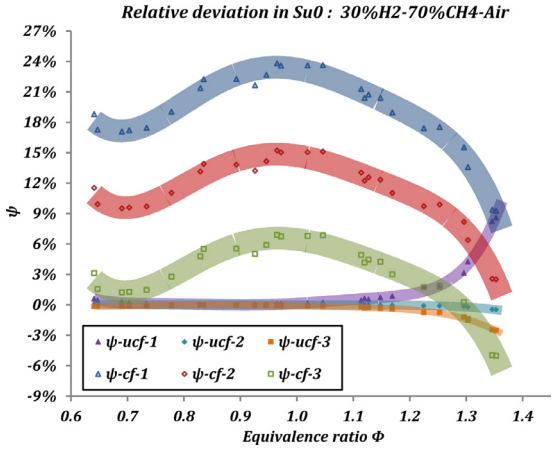

Fig. 9. Relative deviation in burning velocity obtained by different methods and models. Mixture: 70% CH_4–30% H_2–air.

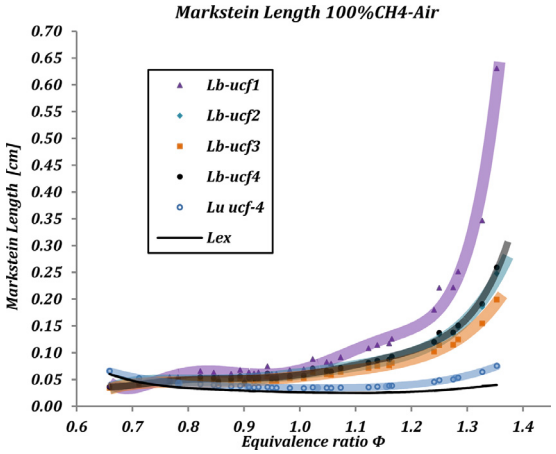

Fig. 10. Markstein lengths of CH_4–air mixtures.

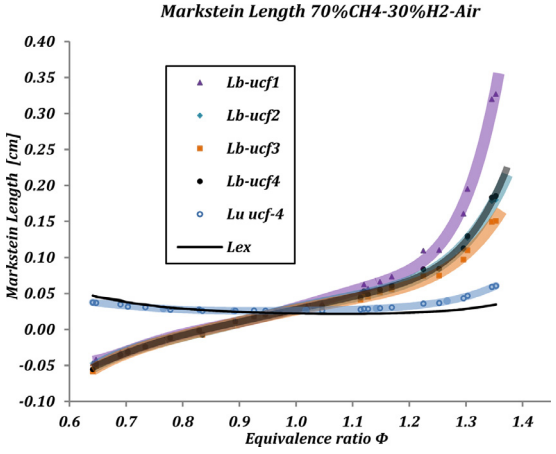

Fig. 11. Markstein length of 70%CH_4–30%H_2–air mixtures.

When considering the burning velocities obtained with the confined flame method, several trends can be observed. First, it can be seen in Figs. 6–10 that using the linear x–P approximation overestimates the burning velocity upon that obtained with the analytical x–P relation –see $\psi_{\text{-}cf\text{-}1}$ and $\psi_{\text{-}cf\text{-}2}$. It can also be seen that when the k_{br} parameter is used, the obtained burning velocity is

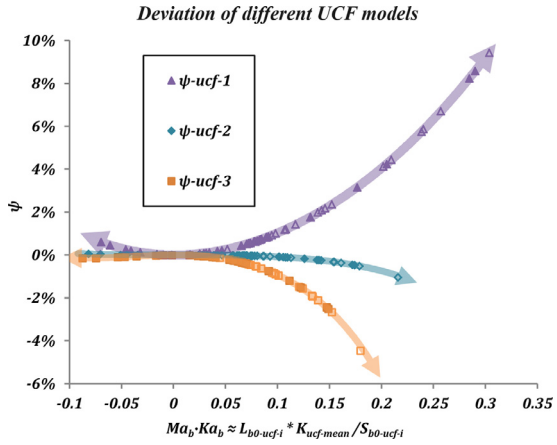

Fig. 12. Relative deviation between different unconfined flame models as function of $Ma_b \cdot Ka_b \approx L_{b0\text{-}ucf\text{-}i} * K_{ucf\text{-}mean} / S_{b0\text{-}ucf\text{-}i}$. Filled symbols: CH_4–air mixture; open symbols: 70%CH_4–30%H_2–air mixture.

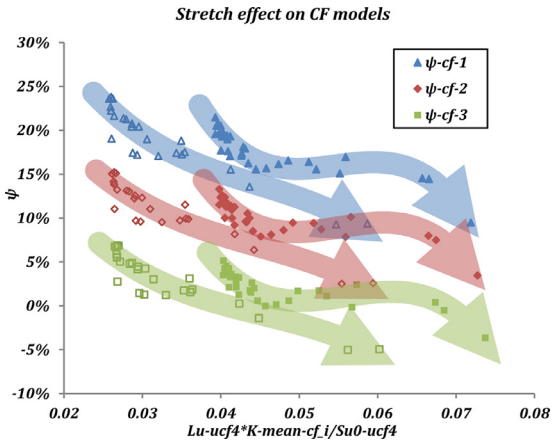

Fig. 13. The trend of $\psi_{\text{-}cf\text{-}i}$ as function of $L_{u0}\ \kappa\ /S_{u0\text{-}ucf\text{-}4}$. Filled symbols: CH_4–air mixture; Open symbols: CH_4–H_2–air mixture.

further reduced – see $\psi_{\text{-}cf\text{-}3}$. From sensitivity analysis conducted on $S_{u0\text{-}cf\text{-}2}$ and $S_{u0\text{-}cf\text{-}3}$ with respect to k_u and k_b it can be shown that reducing/increasing k_b by 1% reduces/increases $S_{u0\text{-}cf\text{-}2}$ and $S_{u0\text{-}cf\text{-}3}$ by ~0.68%, and that reducing/increasing k_u by 1% increases/reduces $S_{u0\text{-}cf\text{-}2}$ and $S_{u0\text{-}cf\text{-}3}$ by ~0.16%. In contrast, $S_{u0\text{-}cf\text{-}1}$ reduces/increases by ~0.55% when reducing/increasing k_u by 1%.

To assess whether the reduction of k_{ba} to k_{br} had a positive effect on accuracy of S_{u0} assessment, we should recall how neglecting the stretch in the confined flame method has affected the results, in particular, whether $S_{u0\text{-}cf\text{-}i}$'s were underestimated or overestimated by neglecting stretch. According to Eq. (3), if the $K*L_u$ is positive, we should expect $S_{u0\text{-}cf\text{-}i}$'s to be underestimated, i.e. lower than the stretch-free $S_{u0\text{-}ucf\text{-}i}$'s. Given that K is positive for outwardly expanding flames and that L_u is positive (see Figs. 10 and 11) during the unconfined flame period and hence most likely will remain positive also during the confined flame period, we may expect $S_{u0\text{-}cf\text{-}i}$'s < $S_{u0\text{-}ucf\text{-}i}$'s . Although this is not seen in the results due to a possible bias error, but the trend of reducing k_b has clearly a positive effect towards achieving the latter expectation. The parabolic shape of the $\psi_{\text{-}cf\text{-}i}$'s curves is believed to be due to increased stretch-neglecting effects for the off-stoichiometric mixtures. To asses this issue, we shall develop the following equation based on Eq. 3:

$$\psi_{cf-i} \equiv \frac{S_{u0-cf-i} - S_{u0-ucf-4}}{S_{u0-ucf-4}} \propto L_{u0} \frac{\overline{\kappa}}{S_{u0-ucf-4}} \tag{27}$$

Here $S_{u0\text{-}cf\text{-}i}$ is considered as the stretch affected burning velocity and $S_{u0\text{-}ucf\text{-}4}$ as the stretch-free one. L_u is the unburned Markstein Length as evaluated by Eq. (6) and $\bar{\kappa}$ is the time-averaged stretch rates during the confined flame period evaluated by Eq. (22). $\bar{\kappa}$ was found to range from 13 to 48 1/s for the investigated mixtures. Figure 13 shows the plots of Eq. (27) for both CH_4–air and CH_4–H_2–air mixtures.

As can be seen, the trend indicates that $\psi_{\text{-}cf\text{-}i}$ behaves similar to $L_{u0}\ \bar{\kappa}/S_{u0\text{-}ucf\text{-}4}$, or alternatively $Ma_u Ka_u$. Hence, we may suggest that the parabolic shape of the $\psi_{cf\text{-}i}$ curves in Figs. 8 and 9 are caused by increasing stretch-neglecting effects in the confined flame method.

4. Conclusions

This work investigated the accuracy and trends of the burning velocity values determined by the confined flame method, with respect to the unconfined flame method, which is considered to be more accurate. For each method, several modeling approaches for burning velocity extraction from the measured data were investigated as well.

For the unconfined flame method, the burning velocities extracted using linear stretch relation was overestimated compared to those extracted with non-linear models for increasing values of $|Ma_b Ka_b| \approx |L_{b0}\bar{\kappa}/S_{b0}| \approx |L_{b0}/R_{f\_mean}|$. This was found to be in agreement with previous works [12–17]. The three non-linear stretch relations investigated revealed close results for $|Ma_b Ka_b| < 0.05$.

When the confined flame method was used, the burning velocity was obtained from the measured pressure rise $P(t)$ as described in Section 2.2. The pressure data range appropriate for using was found to be within $10\% < P_r < 55\%$. The lower limit is set by the signal-to-noise limitations in pressure measurement and the upper-limit is imposed by increased heat losses to the vessels wall. Using the linear x–P approximation showed a strong overestimation in the resulting burning velocity, which could be reduced by applying the more accurate analytical x–P relation. Also, it was observed that by reducing the k_b parameter in the analytical x–P relation below the value corresponding to the burned gas state contributed to a further reduction in overestimation and for that approach the burning velocity values obtained by CF method were closest to those obtained by the UCF method. Consequently, reducing the k_b parameter may be considered as a method to counteract the negligence of detailed thermodynamic properties, detailed chemistry, as well as radiation losses in the CF method. Moreover, it was also observed that although mean stretch rates are very low during the confined flame propagation period ($\bar{\kappa} < 45$ 1/s), the stretch effect is not totally negligible even for the low Markstein-number-mixtures used.

We conclude that the analytical confined flame method, if applied as proposed in this work, could be a cost-effective and less labor-intense alternative to the unconfined flame method, when accuracy can be compromised. Reasonable consistency between S_{u0} obtained by both methods may be achieved by proper analysis of the measured pressure curve, provided stretch effects can be neglected in the confined flame period. Stretch effects can be further reduced by increasing the vessel radius. The latter is limited however, because it leads to longer flame propagation duration, subsequent rise of radiation heat losses and possible occurrence of buoyancy and cellularity.

Acknowledgments

Financial support of the Israel Science Foundation (ISF), grant number -1728/12; Israel Ministry of Science, Technology and Space,

grant number 3-10758; The Israel Council for Higher Education and the Nancy and Stephen Grand Technion Energy Program (GTEP) is gratefully appreciated.

Appendix A

The unburned Markstein length as given by [30] and [31]:

$$\frac{L_{u0}}{\delta_{f0}} = \left(\frac{\rho_{u0}}{\rho_{u0}-\rho_{b0}}\right)\ln\left(\frac{\rho_{u0}}{\rho_{b0}}\right) + \left(\frac{\rho_{b0}}{\rho_{u0}-\rho_{b0}}\right)\frac{\beta(Le-1)}{2}\int_0^{(\rho_{u0}-\rho_{b0})/\rho_{b0}}\frac{\ln(1+x)}{x}dx \quad (A.1)$$

The burned Markstein length as given by [30] and [31]:

$$\frac{L_{b0}}{\delta_{f0}} = \left(\frac{\rho_{u0}}{\rho_{u0}-\rho_{b0}}\right)\ln\left(\frac{\rho_{u0}}{\rho_{b0}}\right) + \left(\frac{\rho_{u0}}{\rho_{u0}-\rho_{b0}}\right)\frac{\beta(Le-1)}{2}\int_0^{(\rho_{u0}-\rho_{b0})/\rho_{b0}}\frac{\ln(1+x)}{x}dx \quad (A.2)$$

By defining L_{ex} as following we get:

$$\begin{aligned} L_{ex} &= L_{u0} - \frac{\rho_{b0}}{\rho_{u0}}L_{b0} \\ &= \delta_{f0}\left(\frac{\rho_{u0}}{\rho_{u0}-\rho_{b0}}\right)\ln\left(\frac{\rho_{u0}}{\rho_{b0}}\right) - \delta_{f0}\frac{\rho_{b0}}{\rho_{u0}}\left(\frac{\rho_{u0}}{\rho_{u0}-\rho_{b0}}\right)\ln\left(\frac{\rho_{u0}}{\rho_{b0}}\right) \\ &= \delta_{f0}\ln\left(\frac{\rho_{u0}}{\rho_{b0}}\right)\left[\left(\frac{\rho_{u0}}{\rho_{u0}-\rho_{b0}}\right) - \left(\frac{\rho_{b0}}{\rho_{u0}-\rho_{b0}}\right)\right] \\ &= \delta_{f0}\ln\left(\frac{\rho_{u0}}{\rho_{b0}}\right) \end{aligned} \quad (A.3)$$

Supplementary materials

Supplementary material associated with this article can be found, in the online version, at doi:10.1016/j.combustflame.2016.03.012.

References

[1] F. Lindström, H.E. Ängström, G. Kalghatgi, C.E. Möller, An empirical SI combustion model using laminar burning velocity correlations, SAE Paper 2005-01-2106.
[2] C.K. Law, C.J. Sung, H. Wang, T.F. Lu, Development of comprehensive detailed and reduced reaction mechanisms for combustion modeling, AIAA J. 41 (2003) 1629–1646.
[3] N. Peters, Laminar flamelet concepts in turbulent combustion, Symp. (Int.) Combust. 21 (1986) 1231–1250.
[4] H. Yu, W. Han, J. Santner, X. Gou, C.H. Sohn, Y. Ju, Z. Chen, Radiation-induced uncertainty in laminar flame speed measured from propagating spherical flames, Combust. Flame 161 (2014) 2815–2824.
[5] J. Jayachandran, R. Zhao, F. Egolfopoulos, Determination of laminar flame speed using stagnation and spherically expanding flames: molecular transport and radiation effects, Combust. Flame 161 (2014) 23065–22316.
[6] J. Santner, F.M. Haas, Y. Ju, F.L. Dryer, Uncertainties in interpretation of high pressure spherical flame propagation rates due to thermal radiation, Combust. Flame 161 (2014) 147–153.
[7] Z. Chen, On the accuracy of laminar flame speeds measured from outwardly propagating spherical flames: methane air at normal temperature and pressure, Combust. Flame 162 (2015) 2442–2453.
[8] F.N. Egolfopoulos, N. Hansen, Y. Ju, K. Kohse-Hoinghaus, C.K. Law, F. Qi, Advances and challenges in laminar flame experiments and implications for combustion chemistry, Prog. Energy Combust. Sci. 43 (2014) 36–67.
[9] Z. Chen, Effects of radiation and compression on propagating spherical flames of methane/air mixtures near the lean flammability limit, Combust. Flame 157 (2010) 2267.
[10] E. Varea, V. Modica, A. Vandel, B. Renou, Measurement of laminar burning velocity and Markstein length relative to fresh gases using a new postprocessing procedure: application to laminar spherical flames for methane, ethanol and isooctane/air mixtures, Combust. Flame 159 (2012) 577–590.
[11] S. Balusamy, A. Cessou, B. Lecordier, Direct measurement of local instantaneous laminar burning velocity by a new PIV algorithm, Exp. Fluids 50 (2011) 1109–1121.
[12] F. Wu, W. Liang, Z. Chen, Y. Ju, C.K. Law, Uncertainty in stretch extrapolation of laminar flame speed from expanding spherical flames, Proc. Combust. Inst. 35 (2015) 663–670.
[13] A.N. Lipatnikov, S.S. Shy, W. Li, Experimental assessment of various methods of determination of laminar flame speed in experiments with expanding spherical flames with positive Markstein lengths, Combust. Flame 162 (2015) 2840–2854.
[14] A.P. Kelley, C.K. Law, Nonlinear effects in extracting laminar flame speed from expanding spherical flames, Combust. Flame 156 (2009) 1844–1851.
[15] Z. Chen, On the extraction of laminar flame speed and Markstein length from outwardly propagating spherical flames, Combust. Flame 158 (2011) 291–300.
[16] F. Halter, T. Tahtouh, C. Mounaïm-Rousselle, Nonlinear effects of stretch on the flame front propagation, Combust. Flame 157 (2010) 1825–1832.
[17] A.P. Kelley, J.K. Bechtold, C.K. Law, Premixed flame propagation in a confining vessel with weak pressure rise, J. Fluid Mech. 691 (2012) 26–51.
[18] M.P. Burke, Y. Ju, Z. Chen, F.L. Dryer, Effects of cylindrical confinement on the determination of laminar flame speeds using outwardly propagating flames, Combust. Flame 156 (2009) 771.
[19] Z. Chen, M.P. Burke, Y. Ju, Effects of compression and stretch on the determination of laminar flame speeds using propagating spherical flames, Combust. Theory Model. 13 (2) (2009) 343–364.
[20] D. Bradley, R.A. Hicks, M. Lawes, C.G.W. Sheppard, R. Woolley, The measurement of laminar burning velocities and Markstein numbers for iso-octane–air and iso-octane–n heptane–air mixtures at elevated temperatures and pressures in an explosion bomb, Combust. Flame 115 (1998) 126–144.
[21] Z. Chen, Y. Ju, Theoretical analysis of the evolution from ignition kernel to flame ball and planar flame, Combust. Theory Model. 11 (2007) 427–453.
[22] Khizer Saeed, C.R. Stone, Measurements of the laminar burning velocity for mixtures of methanol and air from a constant-volume vessel using a multi–zone model, Combust. Flame 139 (2004) 152–166.
[23] S.P. Marshall, R. Stone, C. Heghes, T.J. Davies, R.F. Cracknell, High pressure laminar burning velocity measurements and modelling of methane and n-butane, Combust. Theory Model. 14 (4) (2010) 519–540.
[24] A. Moghaddas, K. Eisazadeh-Far, H. Metghalchi, Laminar burning speed measurement of premixed n-decane/air mixtures using spherically expanding flames at high temperatures and pressures, Combust. Flame 159 (2012) 1437–1443.
[25] M. Metghalchi, J.C. Keck, Burning velocities of mixtures of air with methanol, isooctane, and indolene at high pressure and temperature, Combust. Flame 48 (1982) 191–210.
[26] C. Xiouris, T. Ye, J. Jayachandran, F.N. Egolfopoulos, Laminar flame speeds under engine-relevant conditions: uncertainty quantification and minimization in spherically expanding flame experiments, Combust. Flame 163(2016) 270–283.
[27] C.C.M. Luijten, E. Doosje, L.P.H. de Goey, Accurate analytical models for fractional pressure rise in constant volume combustion, Int. J. Thermal Sci. 48 (2009) 1213–1222.
[28] G.H. Markstein, Experimental and theoretical studies of flame-front stability, J. Aeronaut. Sci. 18 (1951) 199–209.
[29] G.H. Markstein, Non-steady flame propagation, Pergamon Press, 1964.
[30] L. Frankel, G.I. Sivashinsky, On the effect of thermal expansion and Lewis number in spherical flame propagation, Combust. Sci. Technol. 31 (1983) 131–138.
[31] P. Clavin, Dynamic behavior of premixed flame fronts in laminar and turbulent flows, Prog. Energy Combust. Sci. (1985) 1–59.
[32] B. Karlovitz, D.W. Denniston Jr., D.H. Knapschaefer, F.E. Wells, Studies on turbulent flames, Symp. (Int.) Combust (1953) 613–620.
[33] D. Bradley, P.H. Gaskell, X.J. Gu, Burning velocities, Markstein lengths, and flame quenching for spherical methane-air flames: a computational study, Combust. Flame 104 (1996) 176–198.
[34] T. Tahtouh, F. Halter, C. Mounaim-Rousselle, Measurement of laminar burning speeds and Markstein lengths using a novel methodology, Combust. Flame 156 (2009) 1735–1743.
[35] C.K. Wu, C.K. Law, On the determination of laminar flame speed from stretched flames, Symp. (Int.) Combust. 20 (1985) 1941–1949.
[36] D.R. Dowdy, D.B. Smith, S.C. Taylor, A. Williams, The use of expanding spherical flames to determine burning velocities and stretch effects in hydrogen/air mixtures, Symp. (Int.) Combust. 23 (1990) 325–332.
[37] L.K. Tseng, M.A. Ismail, G.M. Faeth, Laminar burning velocities and Markstein numbers of hydrocarbon/air flames, Combust. Flame 95 (1993) 410–426.
[38] K.T. Aung, M.I. Hassan, G.M. Faeth, Flame stretch interactions of laminar premixed hydrogen/air flames at normal temperature and pressure, Combust. Flame 109 (1997) 1–24.
[39] M.I. Hassan, K.T. Aung, G.M. Faeth, Measured and predicted properties of Laminar premixed methane/air flames at various pressures, Combust. Flame 115 (1998) 539–550.
[40] Z. Huang, Y. Zhang, K. Zeng, B. Liu, Q. Wang, D. Jiang, Measurements of laminar burning velocities for natural gas–hydrogen–air mixtures, Combust. Flame 146 (2006) 302–311.
[41] M.I. Hassan, K.T. Aung, G.M. Faeth, Measured and Predicted properties of laminar premixed methane/air flames at various pressures, Combust. Flame 115 (1998) 539–550.
[42] H. Takashi, T. Kimitoshi, Laminar flame speed of ethanol, n-heptane, iso-octane air mixtures, Department of Mechanical Engineering, Oita University, Japan, 2006 F2006SC40.
[43] L. Frankel, G.I. Sivashinsky, On quenching of curved flames, Combust. Sci. Technol. 40 (1984) 257–268.
[44] Z. Chen, M.P. Burke, Y. Ju, Effects of Lewis number and ignition energy on the determination of laminar flame speed using propagating spherical flames, Proc. Combust. Inst. 32 (2009) 1253–1260.

[45] P.D. Ronney, G.I. Sivashinsky, A theoretical study of propagation and extinction of non-steady spherical flame fronts, SIAM J. Appl. Math. 49 (4) (1989) 1029–1046.
[46] X.J. Gu, M.Z. Haq, M. Lawes, R. Woolley, Laminar burning velocity and markstein lengths of methane–air mixtures, Combust. Flame 121 (2000) 41–58.
[47] E.F. Fiock, C.F. Marvin Jr., Frank, R. Caldwell, C.H. Roeder, Flame speeds and energy consideration for explosions in a spherical bomb, National Advisory Committee for Aeronautics, 1940 N.A.C.A. Report No. 682.
[48] K.H. O'Donovan, C.J. Rallis, Determination of the burning velocity of a gas mixture in a spherical constant volume combustion vessel, Combust. Flame 3 (1959) 201–214.
[49] B. Lewis, G. von Elbe, Combustion, flames and explosions of gases, third ed., Academic Press Inc., New York, 1987.
[50] J. Manton, G. von Elbe, B. Lewis, Burning velocity measurements in a spherical vessel with central ignition, Symp. (Int.) Combust. 4 (1) (1953) 358–363.
[51] D. Bradley, A. Mitcheson, Mathematical solutions for explosions multi-zone investigation, Combust. Flame 26 (1976) 201–217.
[52] A.E. Dahoe, L.P.H. de Goey, Laminar burning velocities of hydrogen–air mixtures from closed vessel gas explosions, J. Loss Prev. Process Ind. 18 (2005) 152–166.
[53] E. Monteiro, M. Bellenoue, J. Sotton, N.A. Moreira, S. Malheiro, Laminar burning velocities of typical syngas compositions, Proceedings of the European Combustion Meeting (2009).
[54] C.C.M. Luijten, E. Doosje, J.A. van Oijen, L.P.H. de Goey, Impact of dissociation and end pressure on determination of laminar burning velocities in constant volume combustion, Int. J. Thermal Sci. 48 (2009) 1206–1212.
[55] E. Van den Bulck, Closed algebraic expressions for the adiabatic limit value of the explosion constant in closed volume combustion, J. Loss Prev. Process Ind. 18 (2005) 35–42.
[56] A. Omari, M. Shapiro and L. Tartakovsky, Laminar burning velocity of alcohol reforming products and effects of cellularity on flame propagation, SAE Technical Paper 2015-01-0775, 2015.